Document Number**:** H2020-ICT-52/RISE-6G/D7.2

Project Name:
Reconfigurable **I**ntelligent **S**ustainable **E**nvironments for **6G** Wireless Networks
(RISE-6G)

Deliverable D7.2

Final results on the platform integration and validation

Date of delivery:	30/06/2023	Version:	2.0
Start date of Project:	01/01/2021	Duration:	36 months

Deliverable D7.2

Final results on the platform integration and validation

Project Number:	101017011
Project Name:	**R**econfigurable **I**ntelligent **S**ustainable **E**nvironments for **6G** Wireless Networks

Document Number:	H2020-ICT-52/RISE-6G/D7.2
Document Title:	Final results on the platform integration and validation
Editor(s):	VINCENZO SCIANCALEPORE (NEC)
Authors:	Vincenzo Sciancalepore, Simon He Zhongxia, Placido Mursia, Luca Bastianelli, Valter Mariani Primiani, Youssef Nasser, Maurizio Crozzoli
Dissemination Level:	PU
Contractual Date of Delivery:	30/06/2023
Security:	Public
Status:	Final
Version:	2.0
File Name:	RISE-6G_WP7_D7.2_Final.docx

Abstract

In this deliverable, we provide the latest updates of the experimental hardware and setup for RIS prototypes that will be included and demonstrated within the two RISE-6G field-trials. In particular, we focus on two different application use cases including communication and localization. Available RIS protypes are described and validated for communication and localization use cases separately, including different frequency bands, namely S-band, Ka-band, V-Band and D-band. Finally, we have described the preliminary tests conducted using available RIS prototypes with all corresponding results.

Keywords

Contents

List of Figures

List of Acronyms

5G-NR	5th Generation - New Radio
BER	Bit Error Rate
BS	Base Station
CAPEX	CAPital EXpenditure
CE	Channel Estimation
CSI	Channel State Information
DL	Downlink
DL-DoD	Downlink Direction of Departure
DL-TDoA	Downlink Time Difference of Arrival
DoA	Direction of Arrival
DoD	Direction of Departure
DRL	Deep Reinforcement Learning
EM	Electromagnetic
GDoP	Geometric Dilution of Precision
HRIS	Hybrid Reconfigurable Intelligent Surface
KPI	Key-Performance Indicator
LB-AoI	Localization Boosted - Area of Influence
LE-AoI	Localization Enabled - Area of Influence
LoS	Line-of-Sight
MIMO	Multiple Inputs Multiple Outputs
MISO	Multiple Inputs Single Output
MSE	Mean Squared Error
NMSE	Normalised Mean Squared Error
NVAA	Non-Value-Added Activities
OFDM	Orthogonal Frequency Division Multiplexing
OPEX	OPerating EXpenditure
PARAFAC	PARAllel FACtor
RF	Radio Frequency
R-RIS	Reflective RIS
RT-RIS	Reflective-transmission RIS
RIS	Reconfigurable Intelligent Surface
RSSI	Received Signal Strength Indicator
RTT	Round Trip Time
RT-ToF	Round Trip – Time of Flight
Rx	Receiver
SINR	Signal to Interference plus Noise Ratio
SISO	Single Input Single Output
SLAM	Simultaneous Localization and Mapping
SNR	Signal to Noise Ratio
TDoA	Time Difference of Arrival
ToA	Time of Arrival
Tx	Transmitter
UAV	Unmanned Aerial Vehicle
UE	User
UTDoA	Uplink Time Difference of Arrival
UL	Uplink
UL-DoA	Uplink Direction of Arrival
UL-TDoA	Uplink Time Difference of Arrival

1 Introduction

The RISE-6G project focuses on the ground-breaking technology, namely Reconfigurable Intelligent Surfaces (RIS), which is expected to play a major role in the rollout of the 6th generation (6G) of wireless and mobile networks. In particular, one of the important objectives of RISE-6G is to provide concrete means to demonstrate the feasibility of the proposed technology within different relevant scenarios by designing, building and integrating RIS prototypes and proof-of-concepts (PoCs).

This main objective is fully covered by the work-package 7 (WP7) that analyses and designs an overall RIS-based solution encompassing different RIS-empowered equipment together with advanced transmitters and receivers.

Specifically, this is obtained by assembling and integrating RIS components and fine-tuning realistic equipment settings. Once RIS PoCs are available, they will be installed and exhaustively tested in two different field-trials that account for distinct environmental scenarios. The former is expected to be installed in a real train station, at Rennes, in France where Orange (partner of the project) operates with its own 4G and 5G infrastructure. The latter is expected to be demonstrated in a common kitting scenario, in the CRF (car-OEM, partner of the RISE-6G project) premises where TIM operates its own 5G infrastructure. In both scenarios, RIS will be used to pursue spectral efficiency maximization (or signal coverage), localization accuracy improvement and EMF exposure reduction.

This deliverable will follow up the previous published D7.1 [RISE6G+D71] providing updates about the main RIS-based Proof-of-Concepts analysed and developed in WP3 in the perspective of their functionalities in different use scenarios.

In this deliverable we will summarize the following points:

- Validation of RIS prototypes in a reverberation chamber to emulate real scattering environments;

- Development and integration of RIS prototypes including different frequency bands, such as S-band, Ka-band, V-band and D-band;

- Preliminary results of RIS-empowered networks to pursue communication efficiency maximization and localization accuracy enhancement.

This deliverable is structured as following: after introduction, in-lab experiments are presented with available equipment, RIS hardware and preliminary results within the S-band and Ka-band in Section 2. Proof-of-concepts for V-band and D-band RIS platforms are shown in Section 3, with a preliminary analysis of achieved performance. Finally, Section 4 provides the conclusions and the summary.

1.1 RIS applied to realistic scenarios

We classify Reconfigurable Intelligent Surface (RIS) deployments for potential Proof of Concepts (PoCs) and demonstrators into two main application scenarios: *enhancing communication coverage* (while keeping the ElectroMagnetic Exposure under control) and facilitating and improving *localization accuracy*.

The communication application scenario, depicted in Figure 1-1, serves as a typical illustration. In the context of millimeter-wave communication, transceiver nodes often employ high directional antennas due to limited output power. Consequently, this results in line-of-sight (LoS) communication, which unfortunately restricts deployment flexibility in practical applications. Therefore, the presence of obstacles introduces additional challenges, as these objects can intermittently obstruct or diminish the quality of communication links, causing transitions between LoS and blocked conditions. To address this issue, RIS can be strategically deployed alongside the LoS path. When the primary LoS path is blocked, the RIS can rely on the reflection principle to recover and maintain communication. It acts as a crucial aid for communication resilience and continuity in the face of blockages. It is important to note that different communication devices operating at various operational bands require corresponding RIS components. The choice of RIS controlling strategy, deployment density, and location should be carefully analyzed on a case-by-case basis, taking into consideration the characteristics of the frequency bands involved and the

performance of the RIS prototype. Such considerations play a vital role in optimizing the effectiveness and efficiency of the RIS deployment.
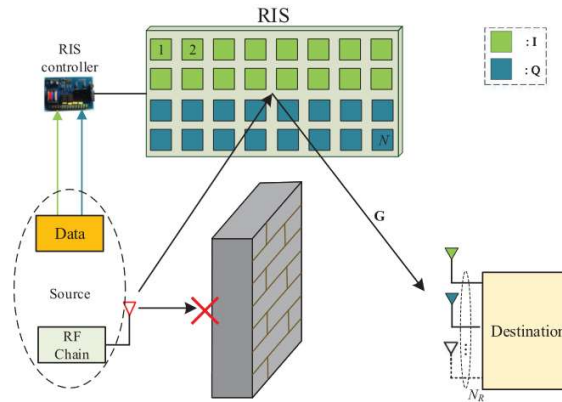
Figure 1-1 : Communication use case for RIS

On the other hand, localization-related use cases will include RIS to form a virtual (passive) scanning beam as shown in Figure 1-2. In a traditional MIMO radar structure, separate radar transceiver channel must be placed with half wavelength spacing in order to form beamforming configuration. For high frequency bands, the antenna element separation gets very limited such that it becomes physically challenging to place full radar transceiver channels in practise. Furthermore, high frequency band transceivers have higher cost and power consumption, therefore traditional MIMO radar concept become less attractive. Using RIS to reflect single radar beam to certain direction can enable high directional virtual scanning beam that enables accurate localization with limited number of expensive millimeter wave transceivers.
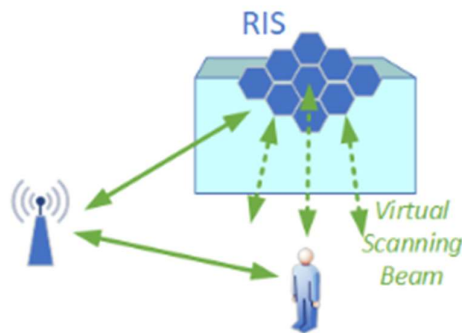
Figure 1-2 : Localization use case for RIS

2 In-lab experiments

2.1 Ancona (CNIT) setup

We have preliminarily tested available RIS prototypes in the reverberation chamber located at CNIT using SDR transmitters as well as 5G commercial base station, provided and maintained by NOKIA. This facility has already been used for emulating real-life scenarios in order to evaluate 4G-LTE system performance as per the following literature: [BMB+17], [MBM+15], [MBC+16], [MBD+18], [MBB+20], [BMD+17], [BMG+14]. Figure 2-1 shows in detail the interior of the considered reverberation chamber.

Figure 2-1. Reverberation chamber used during tests. It is equipped with two stirrers, absorbing materials and, in this case, with the 5G BS module operating at the mm-wave. In addition, on the left side of the chamber there is also the 4G-LTE and 5G (sub-6 GHz) RF modules. Moreover, the user equipment is located within the reverberation chamber and it is connected to a personal computed that collects recorded data.

The reverberation chamber has dimensions 6x4x2.5 m^3. During tests, we can adjust the load within the reverberation chamber, by adding or removing pyramidal absorbers. In this way, the reverberation chamber can be programmatically tuned to emulate the desired environment characterized by proper parameters of a multipath environment, such as the power delay profile and time delay spread [BGM+15, GHR+10].

2.1.1 Ettus USRP B210

We consider a software defined radio (SDR) equipment for our transmitters and receivers. In particular, we use the USRP B210 as shown in Figure 2-2 that provides a fully integrated, single-board, Universal Software Radio Peripheral (USRP™) platform with continuous frequency coverage from 70 MHz to 6 GHz. It is usually designed for low-cost experimental campaigns by combining the AD9361 RFIC direct-conversion transceiver to provide up to 56MHz of real-time bandwidth, an open and reprogrammable Spartan6 FPGA, and fast SuperSpeed USB 3.0 connectivity with convenient bus-power.

The USRP Hardware Driver™ (UHD) software allows to deploy an open-source RAN software, namely srsRAN[1], that emulates the full-stack 4G RAN software to implement base stations (eNB), core domain (EPC) and mobile terminal (UE, according to the 3GPP jargon).

---

[1] https://www.srslte.com/

Figure 2-2. USRP B210 – Software Defined Radio (SDR)

2.1.2 Transmitting antennas

Different antennas are installed on the USRP B210, depending on the intended scenario. Horn antennas as shown in Figure 2-3 are used to perform directive transmissions between transmitter/receiver and RIS.

Figure 2-3. Horn antennas

In addition, external dipole antennas are used to have a uniform energy irradiation in real environments.

2.1.3 4G/5G (NSA) Base Station

We consider the eNode-B and gNode-B as shown in Figure 2-4. Such base stations are effectively installed at CNIT labs in Ancona.
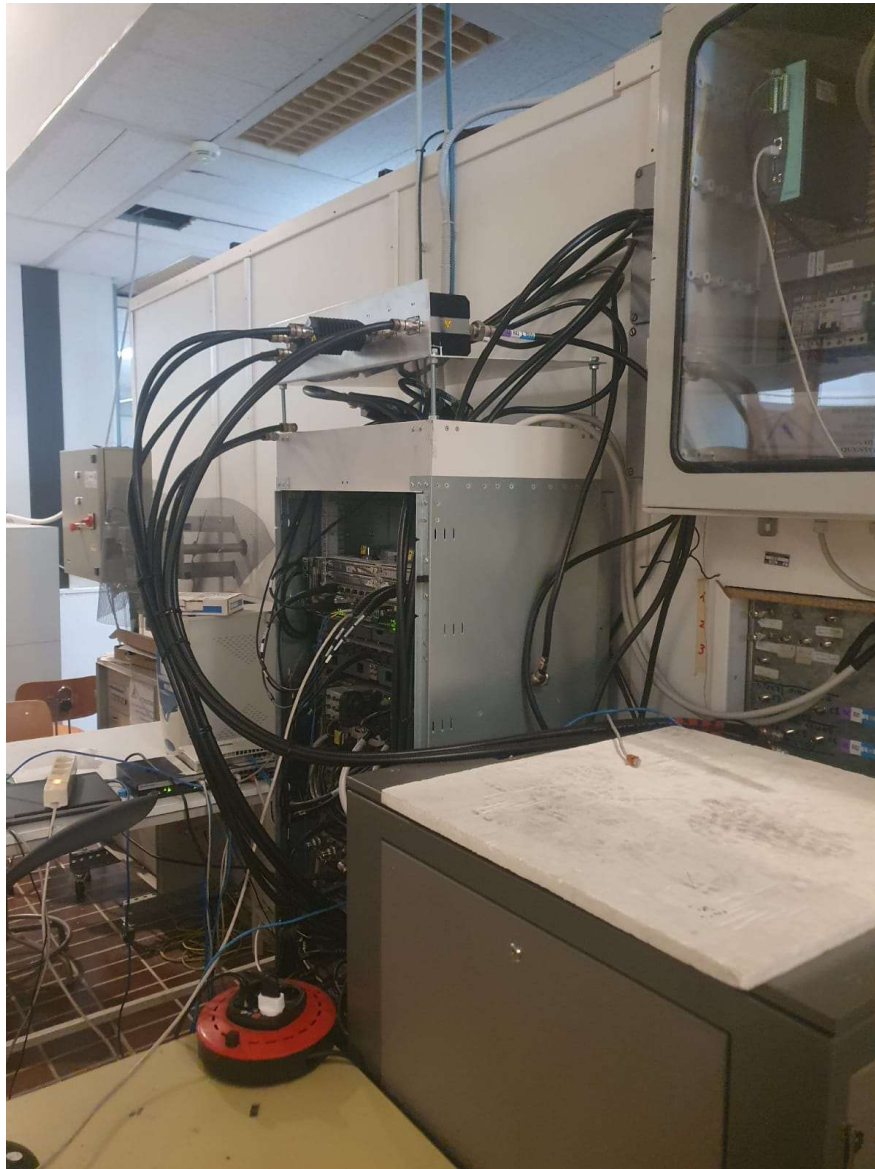
Figure 2-4. 5G Base Station

2.1.4   Sub-6GHz 5G RF module

The 5G RF module operating at N78 band (licensed TIM frequency band is 3720-3800 MHz) installed at CNIT labs in Ancona is shown in Figure 2-5.

Figure 2-5. Sub-6GHz 5G RF module

2.1.5 Mm-waves 5G Base Station

The 5G RF module of Figure 2-6 operates at N258 band (licensed TIM frequency band is 26.9-27.1 GHz) and is installed at CNIT labs in Ancona.

Figure 2-6. mm-waves 5G RF module

2.1.6 4G Base Station

The 4G RF modules operating at B1, B3 and B7 bands are installed at CNIT labs in Ancona as 5G anchor layer and are depicted in Figure 2-7.

Figure 2-7. 4G RF modules

2.1.7 5G User Equipment

User Equipment (UE) is depicted in Figure 2-8 and is installed at CNIT labs in Ancona for enabling end-to-end (E2E) tests.
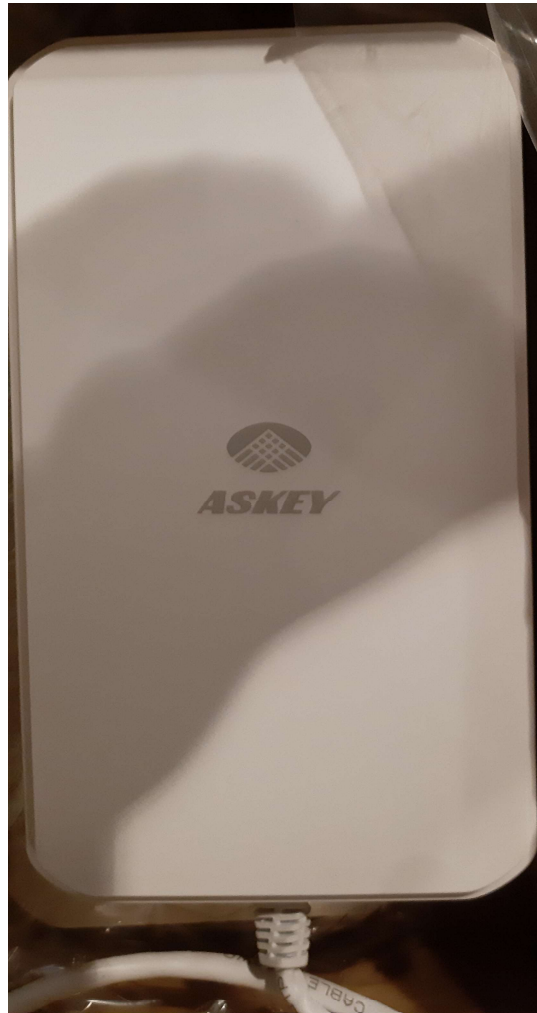
Figure 2-8. 5G User Equipment

2.2 Mm-wave RIS validation (27 GHz)

The preliminary characterization of the chamber at mm-wave in terms of channel properties such as power delay profile, RMS time delay spread, coherence bandwidth and quality factor, has been conducted and reported in work package 3 tasks and reported in the deliverable D3.1 [RISE6G+D31].

Once we have clarified and shown the characteristic of a commercial BS and its corresponding antenna as above-mentioned, we can install the mm-wave RIS provided by Greenerwave (as described in deliverable D7.1 [RISE6G+D71]) within the setup and proceed with an exhaustive measurement campaign.

We consider the antenna with an analog beamforming operating at 26 GHz and the BS able to change dynamically the transmitting beam if there is an obstacle that intercepts the direct beam or if the performance degrades [MDB+23]. This has been realized with the support of BS vendor, namely NOKIA, to prepare our commercial setup to be integrated with a RIS product.

The setup is reported in Figure 2-9, which shows the inner part of the reverberation chamber.
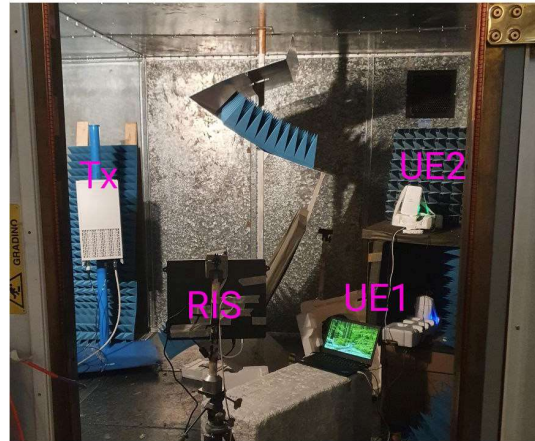
Figure 2-9. Setup designed in WP3 for evaluating the RIS impact when placed within the Reverberation Chamber.

For our evaluation campaign, we consider the following components installed within the reverberation chamber:

- the transmitting antenna (T_x);

- the RIS, placed as shown in Figure 2-10;

- the stirrers (horizontal and vertical) which remain stationary during measurements;

- PC that collects data from the user equipment (UE) labeled as UE_1;

- a second UE, namely UE_2, for simulating another user as per work package 6 activities (not used in those measurements campaign);

- absorbing materials inserted to decrease the Q-factor of the reverberation chamber and needed to replicate a real life scenario, as reported in the deliverable D3.1 [RISE6G+D31].

The UE_1 is surrounded by absorbing material to reduce the multipath contribute due to reflecting walls of the reverberation chamber, thus enhancing the contribute due to the configured RIS.

Figure 2-10. RIS position in the reverberation chamber, in front of the door.

2.2.1   Operational procedure

The RIS has been configured by running an optimization code, which requires as input the coordinates of the T_x and angles of the UE_1 such as azimuth and elevation angle respectively. In such tests, we recorded the reference signals received power (RSRP) at the UE_1 side.

The RSRP was recorded by means of a proprietary software, namely the QXDM, and while recording it, we generated data traffic in order to keep active (and alive) the data link.

We explored two different cases: *i*) the door of the reverberation chamber remains open; *ii*) the door of the reverberation chamber remains close. This last condition is particularly challenging because of the highly reflecting surface introduced by the door just beyond the RIS.

We report our experimental results in Figure 2-11. Hereafter we detail 5 different steps, each of them corresponds to a specific alteration in the RIS-BS configurations.
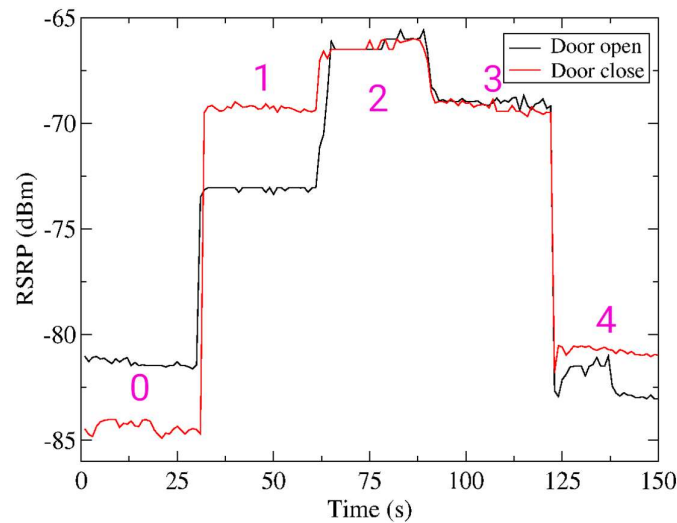
Figure 2-11. RSRP recorded by the UE1.
The graph includes 5 steps, each related to a transition in RIS-BS configurations.

During the acquisition of the RSRP, we perform the following steps:

1. We start from a random configuration of the RIS and activate data traffic;

2. We trigger the optimal configuration of the RIS and the RSRP increases in both cases (data traffic still on);

3. We stop the data traffic;

4. We restart the data traffic;

5. We trigger a random configuration of the RIS.

By exploring that detailed sequence of actions, we can notice that the RIS has a relevant impact on the link connection between the BS and the UE, currently under investigation. The high directivity of the mm-wave system has a relevant impact on these results.

2.3   Sub-6GHz RIS validation (5.3 GHz)

Hereafter, we describe the results obtained during a measurement campaign in the reverberation chamber at the University of Ancona with NEC 10x10 RIS prototype at 5.3 GHz, as described in the deliverable D7.1 [RISE6G+D71].

2.3.1   Measurement setup

The measurement setup is comprised of the NEC RIS prototype, which is placed at the entrance of the reverberation chamber, a horn-antenna transmitter (TX) in the close proximity of the RIS (~1 m from the RIS) and at an angle of -30° from the boresight, and a receiver (RX) placed at ~2.5 m from the RIS and at an angle of 45° from the boresight. The RIS, TX and RX are all placed at the same height.

Moreover, we employ a VNA, which is placed outside of the chamber and connected to both the TX and the RX. The VNA is used to send a single-carrier continuous signal with a transmit power of 10 dBm on the first port, which is connected to the TX, collect the received signal at the second port, which is connected to the RX, and compute the corresponding S_{21} parameter. Such setup is depicted in Figure 2-12.
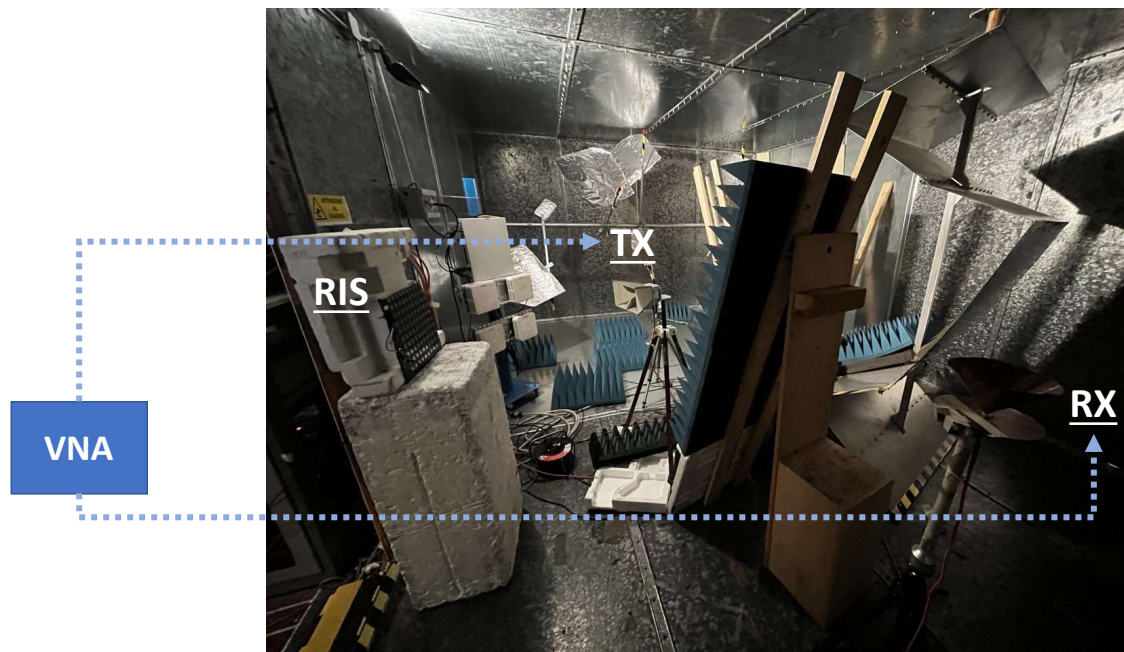
Figure 2-12. NEC RIS measurement setup in the anechoic chamber.

2.3.2   Experiment #1

As a first experiment, we evaluate the performance of the RIS prototype under the best-case scenario, i.e., by utilizing a horn antenna as RX (Figure 2-13). In this regard, we use a pre-defined RIS codebook of configurations, which corresponds to a grid of DFT beams in the range of [-45°,45°] in elevation, and [180°,360°] in azimuth, with a spacing of 5°. Moreover, we exploit the *absorption mode* of this RIS prototype, which corresponds to effectively turning off each RIS cell, as a reference value of the performance in the absence of the RIS.

Figure 2-13. RX horn antenna

We employ the VNA to obtain the S_{21} parameter in dB over a predefined frequency range, and for every configuration in the considered RIS codebook. As depicted in Figure 2-14, we obtain a gain of 7 dB in S_{21} between the best and worst RIS configuration at the working frequency of 5.3 GHz, and a gain of 5 dB from the absorption mode.
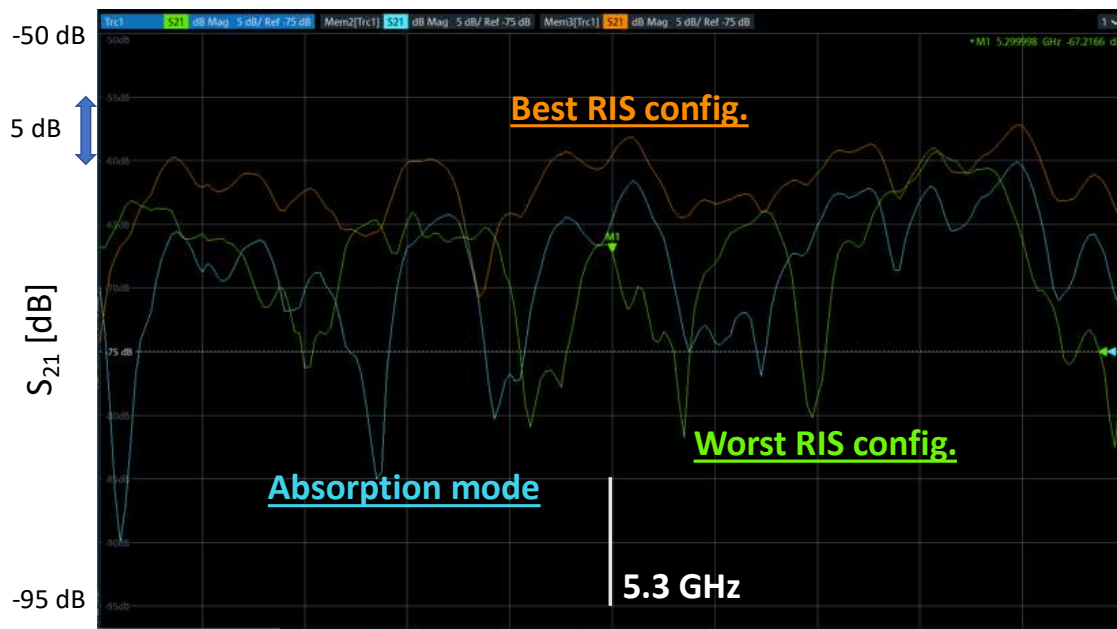
Figure 2-14. Snapshot of the VNA measurement with a horn-antenna RX.

2.3.3 Experiment #2

In the following, we switch the RX to a discone antenna, which represents a much more realistic setting for the end-user, as shown in Figure 2-15. Note that this type of antenna has a uniform radiation pattern in 3D, meaning that it captures all the multipath in the environment.

Figure 2-15. Discone antenna RX

In Figure 2-16, we show the S_{21} in dB for different RIS configurations, by taking the VNA sample corresponding to the RIS operating frequency of 5.3 GHz. Here, we observe a maximum difference between RIS configurations of 6dB, and a gain of 1.5 dB compared to the absorption mode. The best RIS configuration is represented by the beam pointing to 265° and 15° in the azimuth and elevation, respectively.
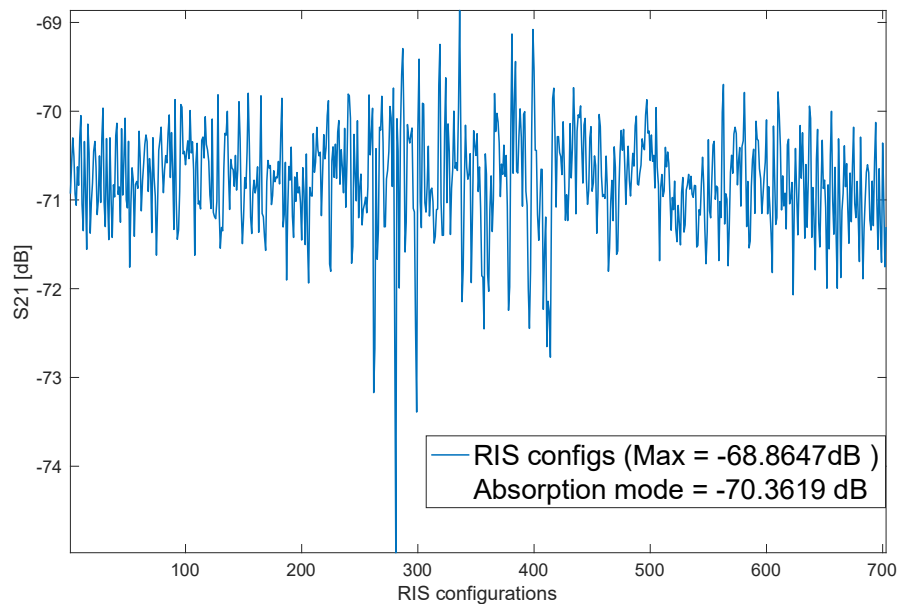
Figure 2-16. S_{21} in dB for different RIS configurations and with discone-antenna RX.

2.3.4 Experiment #3

Given the chaotic environment in the anechoic chamber, we build and tested a randomized RIS codebook in the following way: starting from the best RIS configuration as obtained from experiment #2, dubbed as baseline configuration, we build 700 randomized configurations by changing the state of each RIS unit cell with a fixed probability. As depicted in Figure 2-17, this allows us to obtain a further 1.4 dB gain over the baseline configuration, and a total of 2.9 dB from the absorption mode.
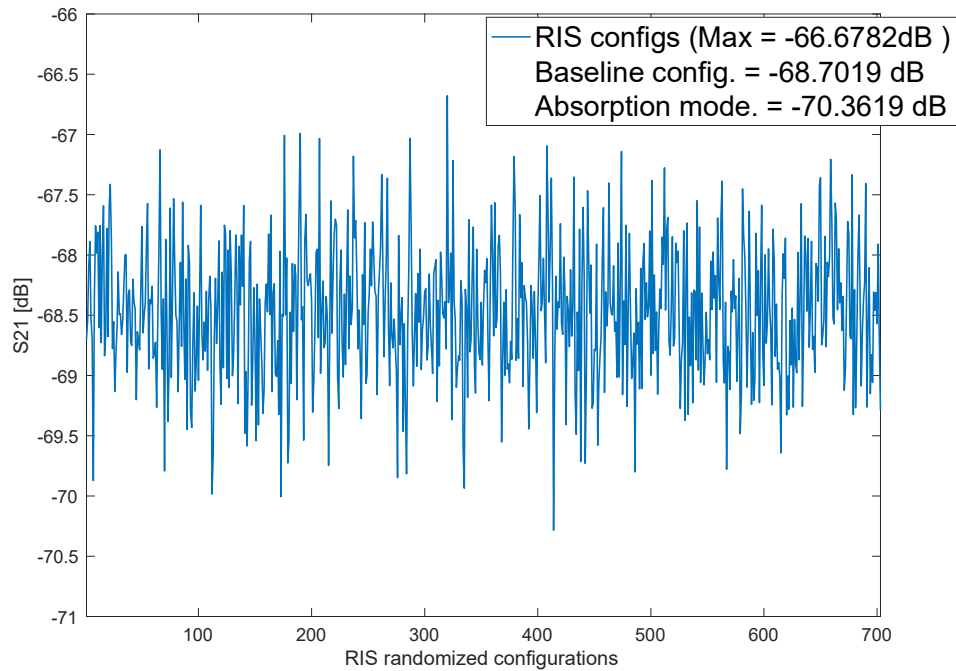
Figure 2-17. S$_{21}$ in dB for different randomized RIS configurations and with discone-antenna RX.

2.3.5 Experiment #4

As a last experiment, we tested the performance of the RIS under varying channel conditions. To this end, we exploit a remotely controlled rotating structure, dubbed as *stirrer*, as depicted in Figure 2-18. This structure rotates at a speed of 1° per second, while the VNA keeps collecting measurements.
As shown in Figure 2-19, we tested 4 different RIS configurations and demonstrated the variability of the S$_{21}$ over time.
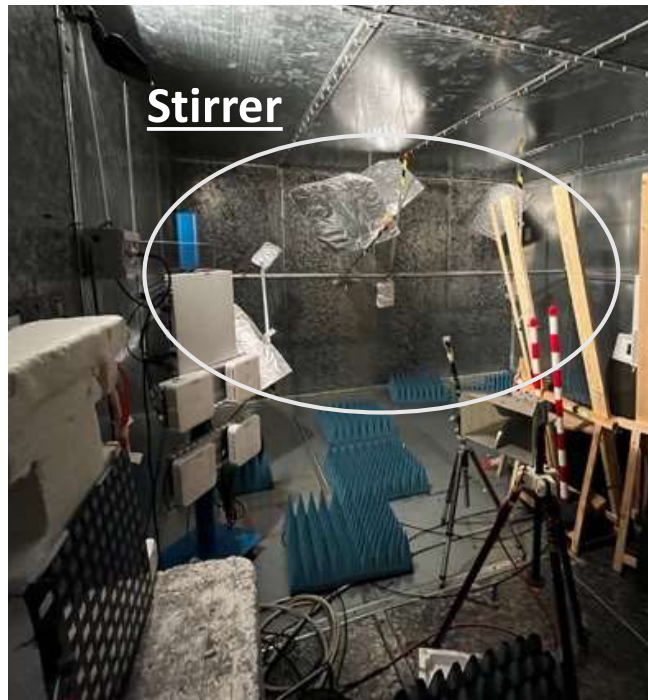
Figure 2-18. Stirrer rotating structure
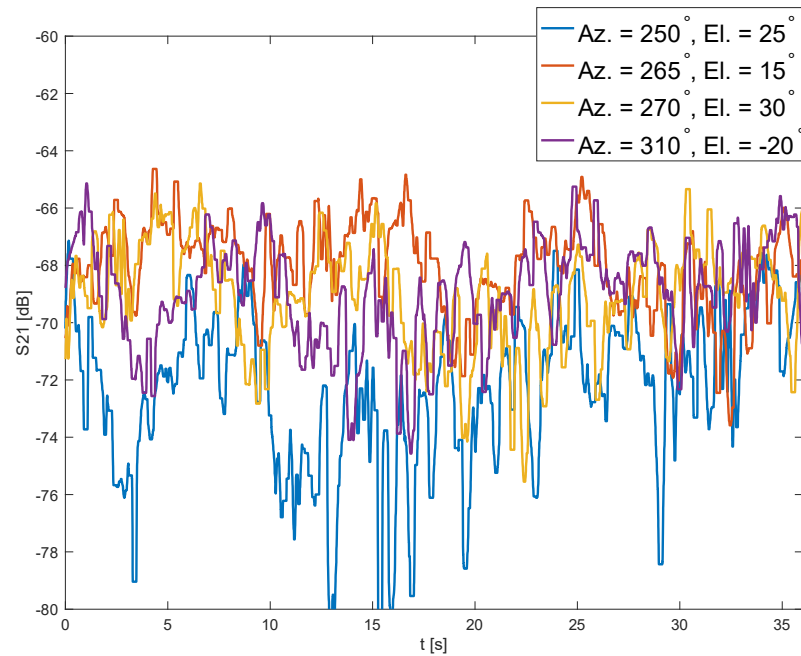
Figure 2-19. S$_{21}$ in dB over time for different RIS configurations and rotations of the stirrer.

3   RIS Proof-of-Concepts

3.1   V-band RIS validation (60 GHz)

Chalmers made V-band RIS by modifying commercial V-band transceiver. The RIS has 16x4 beamforming antenna at both transmitter and receiver side respectively. The RIS can be configured for down-conversion V-band signal and then re-transmitted back at same frequency, thanks to the common local oscillator design share between transmitter and receiver chain, as shown in Figure 3-1.

Both transmitter and receiver have 1GHz baseband bandwidth and RF bandwidth from 58-71 GHz. Adding additional delay network and filter between received IQ ports and retransmission IQ input, additional phase compensation can be made for additional beamforming.
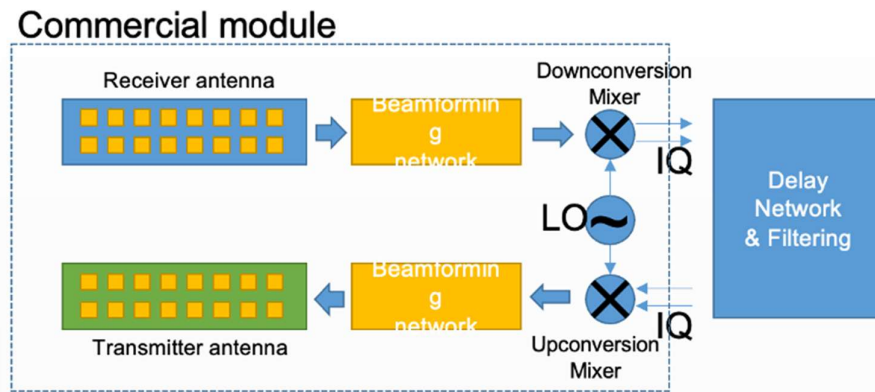
Figure 3-1. Block diagram of proposed V-band RIS prototype

The detail of the antenna array is shown in Figure 3-2. The V-band RIS can be operated at 58-71GHz and receiver and transmitter beamforming of +/-20 degree with 1 degree resolution. The expected beamforming radiation patterns are plotted as well.
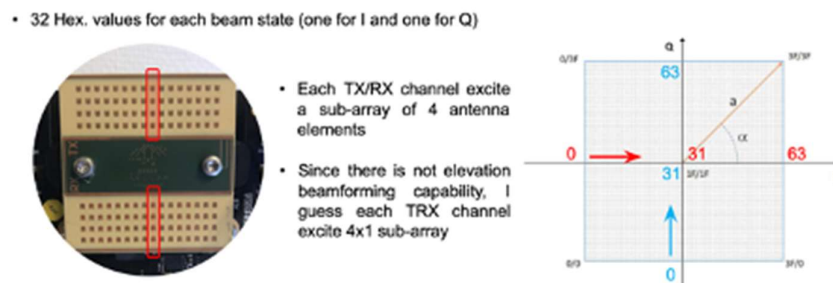
Figure 3-2. Antenna array for V-band RIS
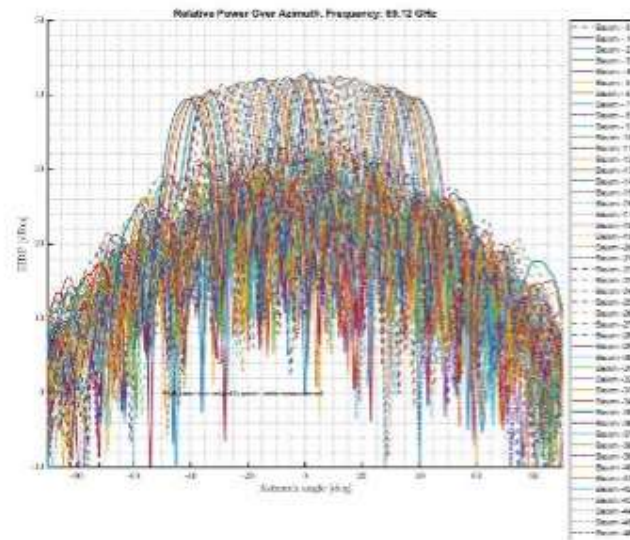
Figure 3-3. Antenna beamforming state adjustment and radiation pattern

3.2 D-band RIS validation (140 GHz)

A D-band RIS unit cell is designed and fabricated in a 130nm SiGe BiCMOS process by Infineon. The design uses two bipolar transistors in a pi-network configuration for impedance manipulation as shown in Figure 3-4. The Chip design also contains a D-band on-chip antenna. Using two controlling bias voltage, the reflectivity phase of RIS unit can be adjusted from 0-180 degree at 140 GHz. The size of the unit cell is 0.75mm X 0.93mm.
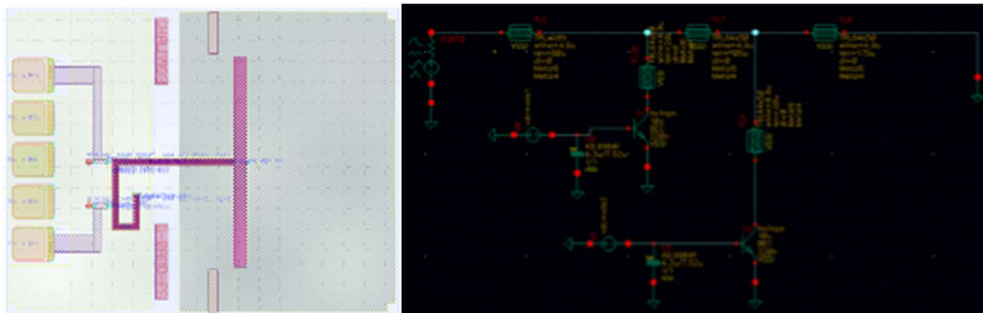
Figure 3-4. D-band RIS Unit Cell MMIC design

The designed RIS phase adjustment performance versus different bias condition is shown in Figure 3-5, with 120-160GHz frequency coverage.
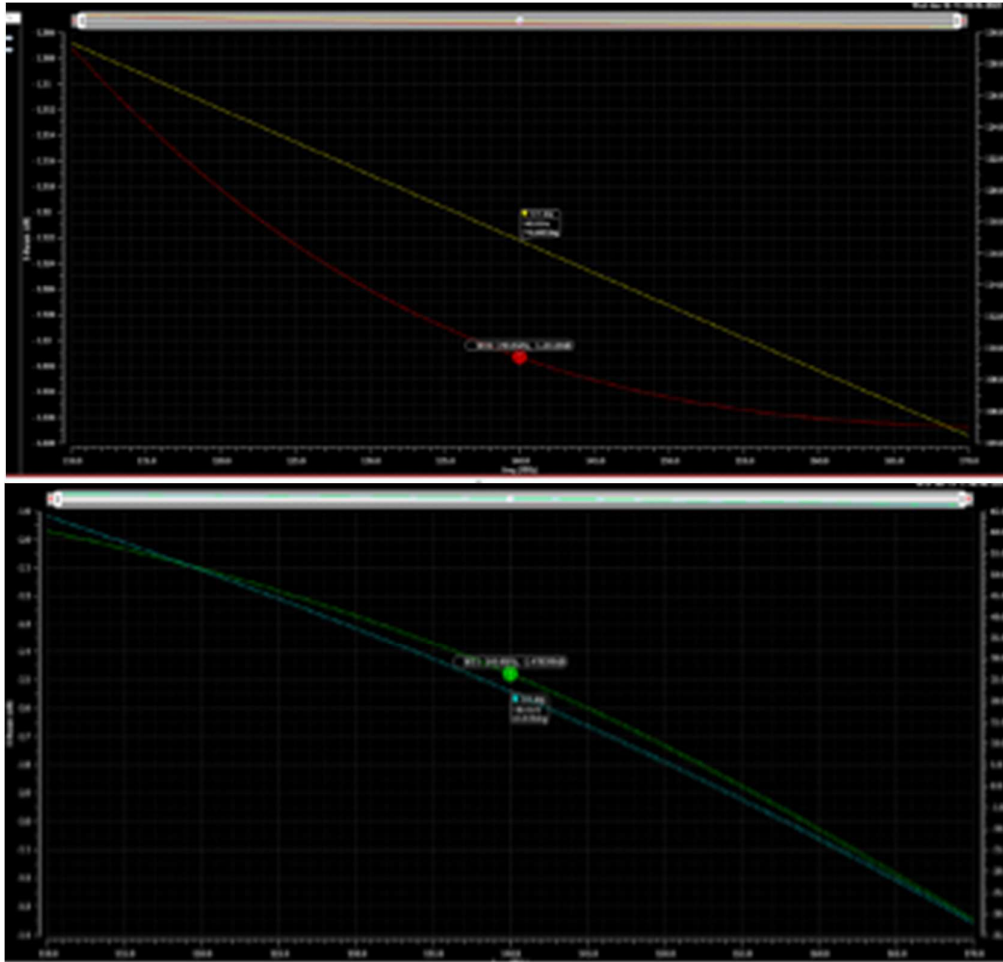
Figure 3-5. D-band RIS unit cell simulation result

The unit cell with on-chip antenna can be also partially inserted into a waveguide to form MMIC to waveguide port interfacing for connecting with a higher gain antenna. The assembly concept is shown in Figure 3-6.
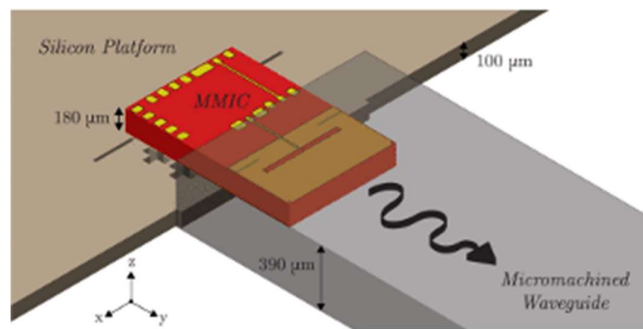
Figure 3-6. D-band RIS unit cell assembly into waveguide concept.

3.3   RIS Hardware Integration for Communication
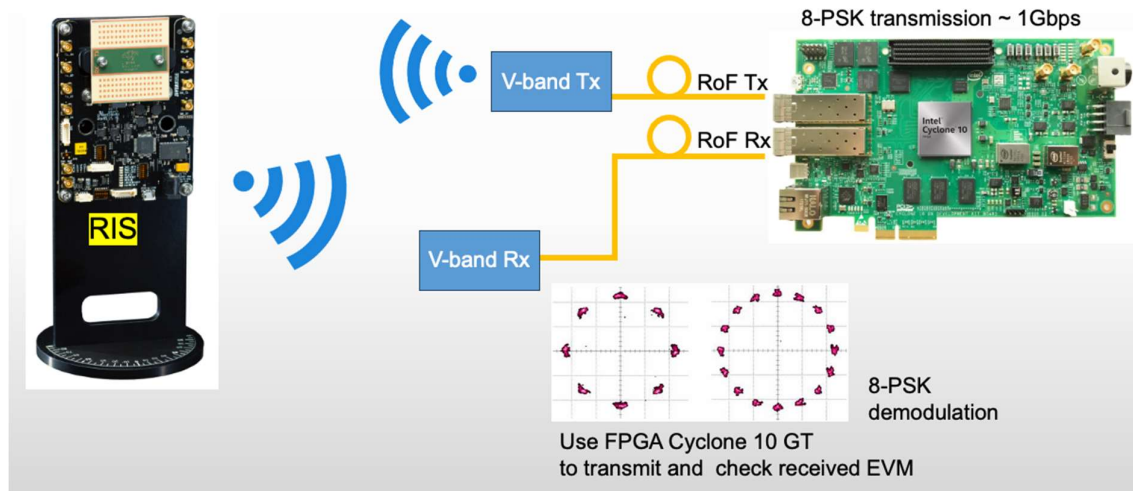
Figure 3-7. RIS PoC integration for Communication

A V-band RIS is used to relay communication when the transmitter and receiver are in non-LoS condition. When transmitter and receiver are setup in NLOS condition, for example at different corner of the room, or direct path is blocked, the communication cannot be sustained due to high path loss. An RIS can be setup in the corner acting as smart reflector to re-establish LoS towards transmitter and receiver respectively.

In this communication test as depicted in Figure 3-7, the transmitter and receiver are located 3 meters away from the RIS. An FPGA is used to generate 8PSK modulated signal at 325 MHz IF frequency with symbol rate of 325 Mbaud symbol rate, which yields 975 Mbps effective date rate. The FPGA using sigma-delta modulation with 10 Gsps sampling rate to generate such 8PSK modulation signal. The IF modulated signal passes fiber and fed into V-band transmitter. On the receiver side, the received IF signal is feedback to the same FPGA via fiber, RoF receiver also acting as 1-bit sampler at 10Gsps and the digitized data is processed by the FPGA for carrier recovery, symbol recovery and received signal bit-error-rate and EVM evaluation. The carrier and symbol recovery algorithm were in [Zhang22].
Experimental shows that EVM < 13% and BER < 10^{-8} when RIS receiver and transmitter beamforming are adjusted correctly towards both transmitter and receiver.

3.4 RIS Hardware Integration for Localization
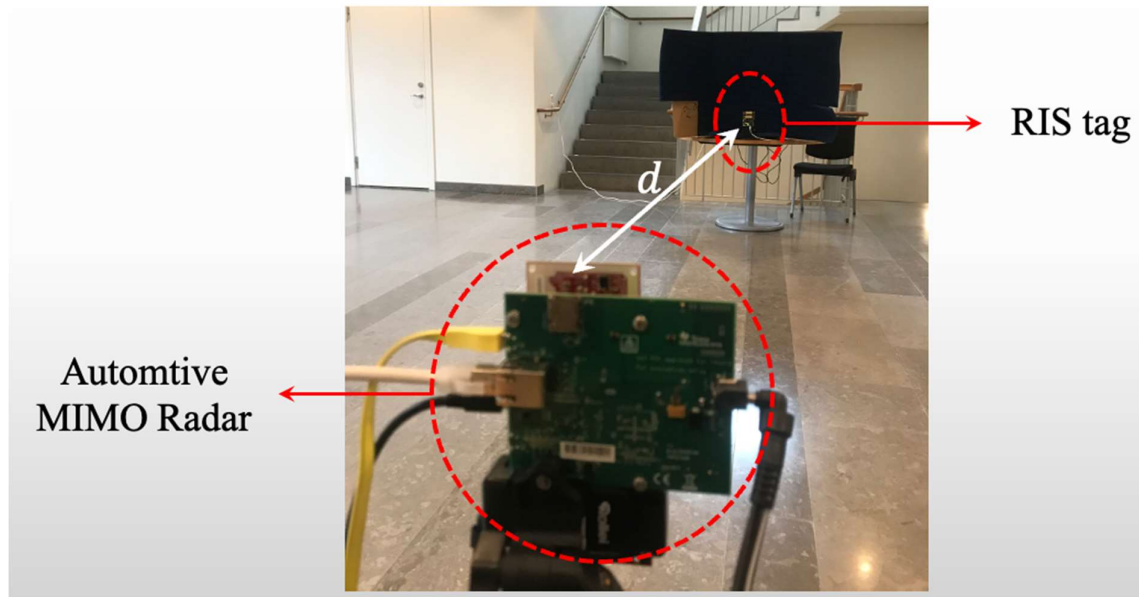
Figure 3-8. RIS PoC integration for Localization

The V-band RIS is also used as active tag together with commercial 60 GHz MIMO radar. When MIMO radar used indoor, multiple reflection from wall and other objects indoor creates multiple unwanted false targets which limits radar detection performance. When active RIS tag is added into the scenario as shown in Figure 3-8, the active RIS can increase the RCS of the target of interesting, thus made it easier to identify this target of interest from false reflections.

The RIS is placed 4.37 meters away from the radar, and the RIS is power off and on respectively to exam the performance. The measurement plots are shown in Figure 3-9.
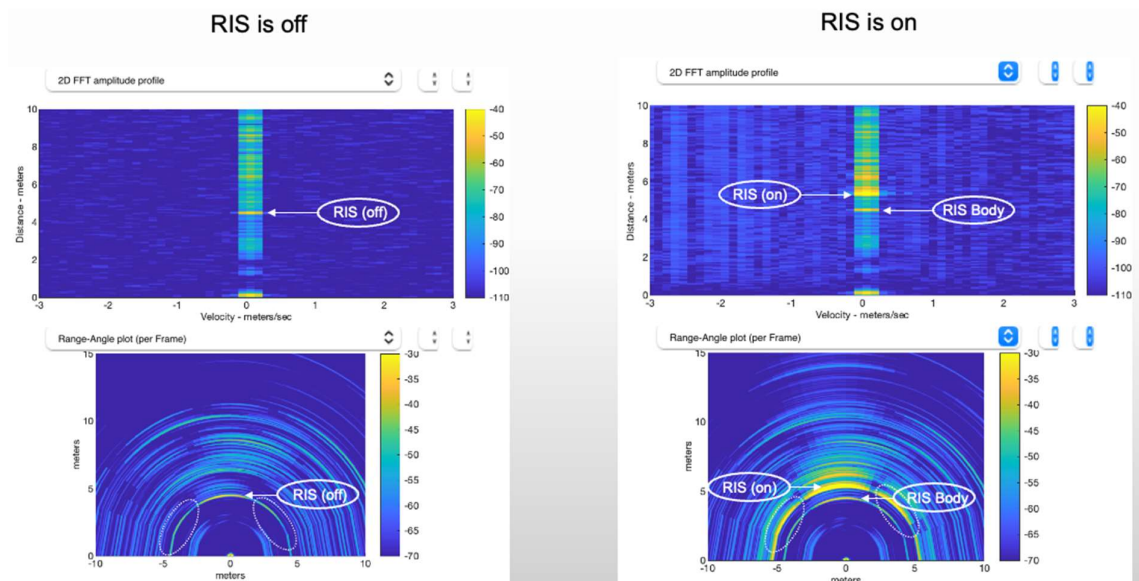
Figure 3-9. Measurement plots for V-band RIS

It can be seen that when RIS is off, the body of the RIS can be detected however with same RCS as surrounding targets, and from 2D plot it is not straightforward to identify the target. When RIS is on, The RIS acts as active reflector, due to cable delay, an additional target with 10dB higher SNR is detected at half meter away from the RIS real position, however, the higher SNR is beneficial for separating the target from multipath reflections.

4 Conclusions and outlook

In this deliverable, we have presented the final results on RIS PoCs among all available RIS prototype developments. In particular, we have selected a subset of available prototype to analyze their performance characterizations. With in-lab tests and field-trial for both communication use-case and localization use-case, we could collect preliminary results. Such RIS prototypes cover wide frequency range, including sub-6GHz and mm-wave, up to 140 GHz. Integrated RIS platforms will be used and demonstrated in two real environments as it will be reported in the deliverable D7.3 [RISE6G+D73].

References

[MDS+21]	P. Mursia, F. Devoti, V. Sciancalepore and X. Costa-Pérez, "RISe of Flight: RIS-Empowered UAV Communications for Robust and Reliable Air-to-Ground Networks," in *IEEE Open Journal of the Communications Society*, vol. 2, pp. 1616-1629, 2021.
[MSG+21]	P. Mursia, V. Sciancalepore, A. Garcia-Saavedra, L. Cottatellucci, X. C. Pérez and D. Gesbert, "RISMA: Reconfigurable Intelligent Surfaces Enabling Beamforming for IoT Massive Access," in *IEEE Journal on Selected Areas in Communications*, vol. 39, no. 4, pp. 1072-1085, April 2021, doi: 10.1109/JSAC.2020.3018829.
[MFC+21]	E. Moro, I. Filippini, A. Capone and D. De Donno, "Planning Mm-Wave Access Networks With Reconfigurable Intelligent Surfaces," *2021 IEEE 32nd Annual International Symposium on Personal, Indoor and Mobile Radio Communications (PIMRC)*, 2021, pp. 1401-1407.
[BMB+17]	M. Barazzetta et al., "A Comparison Between Different Reception Diversity Schemes of a 4G-LTE Base Station in Reverberation Chamber: A Deployment in a Live Cellular Network," in IEEE Transactions on Electromagnetic Compatibility, vol. 59, no. 6, pp. 2029-2037, Dec. 2017, doi: 10.1109/TEMC.2017.2657122.
[MBM+15]	D. Micheli, M. Barazzetta, F. Moglie and V. Mariani Primiani, "Power Boosting and Compensation During OTA Testing of a Real 4G LTE Base Station in Reverberation Chamber," in IEEE Transactions on Electromagnetic Compatibility, vol. 57, no. 4, pp. 623-634, Aug. 2015, doi: 10.1109/TEMC.2015.2434277.
[MBC+16]	D. Micheli, M. Barazzetta, C. Carlini, R. Diamanti, V. M. Primiani and F. Moglie, "Testing of the Carrier Aggregation Mode for a Live LTE Base Station in Reverberation Chamber," in IEEE Transactions on Vehicular Technology, vol. 66, no. 4, pp. 3024-3033, April 2017, doi: 10.1109/TVT.2016.2587662.
[MBD+18]	D. Micheli et al., "Over-the-Air Tests of High-Speed Moving LTE Users in a Reverberation Chamber," in IEEE Transactions on Vehicular Technology, vol. 67, no. 5, pp. 4340-4349, May 2018, doi: 10.1109/TVT.2018.2795650.
[MBB+20]	V. M. Primiani et al., "Reverberation chambers for testing wireless devices and systems," in IEEE Electromagnetic Compatibility Magazine, vol. 9, no. 2, pp. 45-55, 2nd Quarter 2020, doi: 10.1109/MEMC.2020.9133241.
[MDB+23]	D. Micheli et al., "Test of 5G System in the Reverberation Chamber at mm-wave," 2023 17th European Conference on Antennas and Propagation (EuCAP), Florence, Italy, 2023, pp. 1-4, doi: 10.23919/EuCAP57121.2023.10133586.
[BMD+17]	M. Barazzetta, D. Michel, R. Diamanti, L. Bastianelli, F. Moglie and V. M. Primiani, "Optimization of 4G wireless access network features by using reverberation chambers: Application to high-speed train LTE users," 2016 46th European Microwave Conference (EuMC), 2016, pp. 719-722, doi: 10.1109/EuMC.2016.7824444.
[BMG+14]	M. Barazzetta, D. Micheli, P. Gianola, F. Moglie and V. Mariani Primiani, "4G-LTE base station output power estimation from statistical counters during over-the-air tests in reverberation chamber," 2014 International Symposium on Electromagnetic Compatibility, 2014, pp. 284-289, doi: 10.1109/EMCEurope.2014.6930918.
[BGM+15]	L. Bastianelli, L. Giacometti, V. M. Primiani and F. Moglie, "Effect of absorber number and positioning on the power delay profile of a reverberation chamber," 2015 IEEE International Symposium on Electromagnetic Compatibility (EMC), 2015, pp. 422-427, doi: 10.1109/ISEMC.2015.7256199.

[GHR+10]	E. Genender, C. L. Holloway, K. A. Remley, J. M. Ladbury, G. Koepke and H. Garbe, "Simulating the Multipath Channel With a Reverberation Chamber: Application to Bit Error Rate Measurements," in IEEE Transactions on Electromagnetic Compatibility, vol. 52, no. 4, pp. 766-777, Nov. 2010, doi: 10.1109/TEMC.2010.2044578.
[GLL+22]	J.B. Gros, G. Lerosey, F. Lemoult, M. Lodro, S. Greedy, and G. Gradoni. "Multi-path fading and interference mitigation with Reconfigurable Intelligent Surfaces." https://arxiv.org/abs/2206.08290.
[LGG+22]	M. Lodro, J.B. Gros, S. Greedy, G. Lerosey, A. Al Rawi, and G. Gradoni. "Experimental Evaluation of Multi-operator RIS-assisted Links in Indoor Environment." https://arxiv.org/abs/2206.07788.
[RMG+22]	M. Rossanese, P. Mursia, A. Garcia-Saavedra, V. Sciancalepore, A. Asadi, and X. Costa-Perez, "Designing, Building, and Characterizing RF Switch-based Reconfigurable Intelligent Surfaces", in Proceedings of the 16th ACM Workshop on Wireless Network Testbeds, Experimental Evaluation & Characterization (WiNTECH'22), 2022, Sydney, NSW, Australia. [Online]: http://arxiv.org/abs/2207.07121
[RISE6G+D31]	H2020-ICT-52 RISE-6G, "D3.1 - Preliminary RIS model and measurement campaigns", 2022. Online at: https://rise-6g.eu/Documents/LIVRABLES/RISE-6G_WP3_D3.1_Final.pdf
[RISE6G+D32]	H2020-ICT-52 RISE-6G, "D3.2 - RIS designs, and first prototypes characterization", 2023. Online at: https://rise-6g.eu/Documents/LIVRABLES/RISE-6G_WP3_D3.2_Final.pdf
[RISE6G+D71]	H2020-ICT-52 RISE-6G, "D7.1 - Integration methodology and impact measurements through advanced KPIs", 2022. Online at: https://rise-6g.eu/Documents/LIVRABLES/RISE-6G_WP7_D7.1_Final.pdf
[RISE6G+D73]	H2020-ICT-52 RISE-6G, "D7.3 - Final results of PoCs & trials", 2023.